Sulfidation Mechanisms of Fe(III)-(oxyhydr)oxide Nanoparticles: A Spectroscopic Study

Journal:	*Environmental Science: Nano*
Manuscript ID	EN-ART-11-2017-001109.R1
Article Type:	Paper
Date Submitted by the Author:	10-Feb-2018
Complete List of Authors:	Kumar, Naresh; Stanford University, Lezama-Pacheco, Juan; Stanford University, Environmental & Earth System Sciences Noel, Vincent; Stanford Synchrotron Radiation Lightsource Dublet, Gabrielle; EPFL Brown, Gordon; Stanford University

SCHOLARONE™
Manuscripts

Environmental Significance Statement

Fe(III)-(oxyhydr)oxide nanoparticles (*e.g.,* ferrihydrite, goethite, hematite) are effective scavengers of trace metals and various organic and inorganic contaminants from surface and ground waters, soils, and sediments. Sulfidation of these nanoparticles and the nature of iron sulfides formed during this process strongly affect the speciation and mobility of heavy metals (*e.g.*, Cr, Co, Ni, Zn, Cd) metalloids (*e.g.*, As, Se), and actinides (U). Our results reveal that though the reaction is surface controlled, surface area alone does not explain the differences in reactivity of different Fe(III)-(oxyhydr)oxides nanoparticles with dissolved sulfides and atomic-level surface structure is also likely to play an important role.

Sulfidation Mechanisms of Fe(III)-(oxyhydr)oxide Nanoparticles: A Spectroscopic Study

Naresh Kumar[1,2], Juan Lezama Pacheco[3], Vincent Noël[4], Gabrielle Dublet[1,5], and Gordon E. Brown Jr.[1,2,4]

[1]Department of Geological Sciences, School of Earth, Energy, and Environmental Sciences, Stanford University, Stanford, CA 94305-2115, USA

[2]Center for Environmental Implications of NanoTechnology (CEINT), Duke University, P.O. Box 90287, Durham, NC 27708-0287, USA

[3]Department of Earth System Science, School of Earth, Energy, and Environmental Sciences, Stanford University, Stanford CA 94305, USA

[4] Department of Photon Science and Stanford Synchrotron Radiation Lightsource, SLAC National Accelerator Laboratory, 2575 Sand Hill Road, Menlo Park, CA 94025, USA.

[5] Environmental Microbiology Laboratory, Ecole Polytechnique Federale de Lausanne (EPFL), Ch-1015 Lausanne, Switzerland.

*Corresponding author

Naresh Kumar
Department of Geological Sciences
Stanford University,
Stanford CA 94305
nareshk@stanford.edu
(+1) 650 723 7513

Abstract

We used synchrotron-based x-ray absorption spectroscopy, transmission electron microscopy, and wet chemical analyses to study the sulfidation mechanism(s) and sulfur oxidation products from the reaction of ferrihydrite, goethite, and hematite nanoparticles with dissolved sulfide at different S/Fe molar ratios under anaerobic condition. Our results suggest that surface area alone does not explain the differences in reactivity of Fe(III)-(oxyhydr)oxide nanoparticles with dissolved sulfides; differences in atomic-level surface structure are also likely to play an important role. The higher reactivity of ferrihydrite leads to a faster sulfidation rate compared to that of goethite and hematite. We found that polysulfides as well as elemental sulfur are the major reaction products in the sulfidation of all three Fe(III)-(oxyhydr)oxide nanoparticles studied. We also found that thiosulfate and sulfate formed during the sulfidation of goethite and hematite but did not form in the case of ferrihydrite, suggesting that the slower reaction kinetics of goethite and hematite favors the formation of solid-phase thiosulfates and elemental sulfur in our experiments. In addition, our results revealed that the S/Fe ratio is a critical variable in the sulfidation reaction. Iron dissolution rates for ferrihydrite, goethite, and hematite nanoparticles were found to increase up to a S/Fe ratio of ≤ 0.5 and decline above this ratio, suggesting formation of FeS species. Similarly, Fe dissolution rates increased with increasing S/Fe ratios and remained an order of magnitude higher for ferrihydrite than for goethite and three times higher for ferrihydrite than for hematite. Sulfur-*K*-edge x-ray absorption near edge structure (XANES) spectroscopy revealed for the first time the mass distribution of these solid-phase sulfur oxidation products. In addition, we used Fe-*K*-edge XANES and extended x-ray absorption fine structure (EXAFS) spectroscopic analysis to follow the kinetics of FeS formation for the three types of Fe(III)-(oxyhydr)oxide nanoparticles, with varying S/Fe ratios. Ferrihydrite transformed completely to FeS in our experiments, but only 58% of the goethite and only 18% of the hematite transformed to FeS. These results have important environmental implications for Fe- and S-redox cycling and contaminant mobility and provide experimental evidence for the impact of S/Fe ratio on contaminant mobility in the systems studied, either by releasing surface-sorbed contaminants due to Fe(III)-reductive dissolution at lower S/Fe ratios or by trapping or co-precipitation of contaminants with FeS precipitation at higher S/Fe ratios.

1. Introduction

Iron is the most abundant redox-sensitive element on Earth and in oxidizing surface and near-surface environments is commonly present as Fe(III)-(oxyhydr)oxides like ferrihydrite (~$Fe(OH)_3$), goethite (α-FeOOH), and hematite (α-Fe_2O_3). When these phases are in the form of nanoparticles, they are particularly effective scavengers of trace metals and contaminants from surface and ground waters, soils, and sediments[1-5]. Reduction of Fe(III)-(oxyhydr)oxides is a prominent pathway contributing to electron fluxes in subsurface environments[6]. Reductive dissolution of Fe(III)-(oxyhydr)oxides can occur by respiration of iron-reducing bacteria (IRB), by metal-reducing heterotrophic bacteria coupled with oxidation of organic carbon[7,8], as well as by abiotic reduction with H_2S produced by microbial sulfate reduction[9-12]. These types of redox reactions have important geochemical implications due to their key role in iron and sulfur biogeochemical cycles, especially in Fe-sulfide formation. Sulfidation of Fe(III)-(oxyhydr)oxides and consequent reductive dissolution strongly affects the speciation and mobility of heavy metals (*e.g.*, Cr, Co, Ni, Zn, Cd)[13-17], metalloids (*e.g.*, As, Se)[18-21], and actinides (U)[22-24] in sub-surface environments. As a consequence, the formation and behavior of iron-sulfide minerals are central to our understanding of the cycling of Fe and S in the environment.

Deriving a clear understanding of the kinetics and mechanism(s) of sulfidation of Fe(III)-bearing minerals in natural systems is challenging due to the difficulty of determining the different solid phases present, reactive surface areas, and concentrations of dissolved sulfide present in natural samples. During the reaction of dissolved sulfide with Fe(III)-(oxyhydr)oxide nanoparticles, oxidation of sulfide ions at mineral-aqueous solution interfaces causes the release of Fe(II) into solution[25]. The subsequent reaction of Fe(II) with additional dissolved sulfide produces poorly crystalline iron monosulfide (FeS)[25-28] that may eventually convert to more stable products such as pyrite (FeS_2)[26,29-31]. In order to form stoichiometric FeS, two electrons must exchange - one to reduce Fe(III) to Fe(II) and one to bind Fe(II) to dissolved sulfide to

form FeS[25]. Thus, it is the reductive dissolution of Fe(III) to Fe(II) that controls the sulfidation reaction of Fe(III)-(oxyhydr)oxides.

The release of Fe(II) to solution is expected to be controlled by the surface structure and reactive surface area of the Fe(III)-(oxyhydr)oxide phases involved. In addition, Poulton *et al*[32]. found a range in reactivity of Fe(III)-(oxyhydr)oxides with dissolved sulfides, suggesting orders-of-magnitude differences in reactivity for different Fe(III)-(oxyhydr)oxides when normalized to surface area. Overall, the availability of dissolved sulfide in solution under anaerobic conditions will ultimately control the release of Fe(II) into solution and the formation of Fe-sulfide phases. In natural systems, the availability of dissolved sulfide will depend on the rate and extent of microbial sulfate reduction[33] and is ultimately controlled by the availability of organic carbon, ligand exchange, etc.[26,34] and often difficult to estimate. However, a wide range of dissolved sulfide concentrations has been reported in natural environments (*e.g.,* pore water sulfide concentrations of 200-600 $\mu molL^{-1}$ in estuarine sediments[14], 29-209 $\mu molL^{-1}$ in wetland sediments[35], 400-600 $\mu molL^{-1}$ in mangrove sediments[36], and 18.8 $\mu molL^{-1}$ in pore waters collected from acid sulfate soil[37].

It is reasonable to assume that different sulfide-to-iron (S/Fe) ratios will affect the rate and mechanism of the sulfidation reaction and also the types of intermediate sulfur species formed. Intermediate sulfur species, including elemental sulfur (S(0)), polysulfides (S_n(-II)), thiosulfate ($S_2O_3^{2-}$), and sulfite (SO_3^{2-}) are formed due to oxidation of sulfide during reaction with Fe(III)-(oxyhydr)oxide[29,38] and are necessary to convert FeS ultimately into pyrite (FeS_2)[27,38,39]. Although, the mechanism of the reaction between Fe(III)-(oxyhydr)oxides and dissolved sulfide has been the subject of a number of studies and is reasonably well understood[9,28], no study to date has employed a systematic approach to determine the transformations and fates of solid-phase sulfur species that ultimately control the $FeS_{(x)}$ species formed and the rate at which dissolved sulfide is fixed as Fe-sulfide. In addition, there has not

been much discussion about the effect of different S/Fe ratios on the sulfidation reaction of Fe(III)-(oxyhydr)oxides.

In the present study, we assessed the reaction of dissolved sulfide with three types of Fe(III)-(oxyhydr)oxide nanoparticles (ferrihydrite, goethite, and hematite) with different surface areas and crystallinities in batch reactors. Our objective was to understand the mechanism(s) and kinetics of these reactions, with a special focus on monitoring the formation of intermediate, solid-state sulfur species. The dissolved sulfide concentrations in the batch reactors were varied in order to provide a range of different S/Fe molar ratios (0.1 to 2.0) in solution. The reason for using different concentrations of dissolved sulfide was to determine the ideal S/Fe ratio at which FeS precipitation will overcome the process of reductive dissolution of Fe(III) from Fe(III)-(oxyhydr)oxide mineral to Fe(II) in solution. Also of interest is the identity of the intermediate solid sulfur species formed during the sulfidation reactions as well as the concentrations of Fe and sulfate in aqueous solution. As poorly crystalline iron sulfide phases like FeS (mackinawite) and intermediate sulfur species are difficult to analyze using conventional solid-phase techniques (*e.g.*, by x-ray diffraction analysis), we carried out synchrotron-based S-*K*-edge and Fe-*K*-edge x-ray absorption spectroscopy (XAS) to quantitatively identify intermediate sulfur species and to decipher reaction mechanisms.

2. Materials and Analytical Procedures

2.1 Materials

2.1.1 Ferrihydrite synthesis – Synthetic two-line ferrihydrite (Fh) was prepared by titrating a 50mM aqueous solution of ferric nitrate nonahydrate ($Fe(NO_3)_3 \cdot 9H_2O$) (Sigma Aldrich, USA) with a 1M potassium hydroxide (KOH) solution (Fischer Scientific, USA) to pH 6.5 as described by Schwertman and Cornell[40]. After hydrolysis, the precipitates were centrifuged at 12000RPM (Spectrafuge 16M, Labnet International, USA) and the ferrihydrite nanoparticles were washed thoroughly with deionized water to remove traces of nitrate. The freeze-dried powder was stored

in an airtight glass tube at 4°C until further use, and samples were not stored longer than 2 weeks.

2.1.2 Goethite synthesis – Goethite nanoparticles were synthesized using the method described by Schwertman and Cornell[40]. Briefly, 11mM of ferric nitrate nonahydrate ($Fe(NO_3)_3 \bullet 9H_2O$) aqueous solution (Sigma Aldrich, USA) was titrated to pH 12 with a 33mM sodium hydroxide (NaOH) (EMD, Germany) solution. The suspension was kept at 65°C for 48hrs in a temperature-regulated water bath. The suspension turned yellow by the end of 48hr of incubation, and the precipitates were centrifuged at 12000RPM and washed with deionized water at least 5 times to remove extra salts. The sample was then dried in an oven at 40°C and the powder was stored in air-tight glass vials until used.

2.1.3 Hematite synthesis – Hematite nanoparticles were synthesized by adding 0.02M of Fe from ferric nitrate nonahydrate ($Fe(NO_3)_3 \bullet 9H_2O$) aqueous solution (Sigma Aldrich, USA) to 2L of a solution of 0.002M HNO_3 which was constantly stirred and preheated to 98°C before the addition of iron salt as described by Schwertman and Cornell[40]. This mixture was then kept at 98°C for 7 days in an oven. Bright red precipitates were centrifuged and washed 5 times with deionized water before use.

2.1.4 Characterization of nanoparticles – The degree of crystallinity and phase purity of all three Fe(III)-(oxyhydr)oxide nanoparticles were confirmed by x-ray diffraction analysis (**Figure S1;** Supporting Information). Total available surface area of the Fe(III)-(oxyhydr)oxide nanoparticles was determined by the multi-point Brunauer–Emmett–Teller (BET) method using a Micromeritics 2200 BET instrument. Particle sizes of the Fe(III)-(oxyhydr)oxide nanoparticles were measured in solution using a Malvern ZS Zetasizer (**Figure S9**). The measured surface areas and average particle sizes are $332 m^2 g^{-1}$ and ~5nm (ferrihydrite), $36 m^2 g^{-1}$ and ~50-70nm (goethite), and $32 m^2 g^{-1}$ and ~50nm (hematite). Transmission electron microscopy (TEM) was

also used to characterize the morphology and size of nanoparticles (**Figure 8**). Ferrihydrite nanoparticles are irregularly shaped and 5-10 nm in diameter; goethite is present as nanorods that are 70-100 nm in length and 4-6 nm in width; hematite nanoparticles were found to be round in shape and ~50nm in diameter.

2.1.5 Sulfide solution – A stock solution of dissolved sulfide was prepared by dissolving $Na_2S{\bullet}9H_2O$ crystals (Acros, Belgium) in N_2-purged deionized water. Nitrogen-purged water was prepared by bringing the deionized water to the boil and sparging with high purity N_2 gas while cooling down to room temperature (approx. 4hrs).

2.2 Sulfidation Reaction

A total of 200mg of ferrihydrite, goethite, or hematite nanoparticles was placed in 20mL of de-oxygenated deionized water (in 25mL glass vials) with different dissolved sulfide-to-iron ratios (S/Fe = 0.1; 0.2; 0.5; 1.0; and 2.0) under an N_2:H_2 (95:5) atmosphere (COY Industries glove box). Vials were closed with an airtight septum to restrict oxygen exposure. Vials were then slowly shaken (40 RPM) and were sacrificed after 1 day, 5 days, and 14 days inside the N_2-filled glove box. The precipitates were centrifuged (Spectrafuge 16M, Labnet International, USA) inside the glove box and the aqueous solution was stored in 20mL plastic tubes for further chemical analysis. The precipitates were dried under N_2 and kept sealed until analysis for solid-phase identity, including S-*K*-edge and Fe-*K*-edge x-ray absorption spectroscopy.

2.3 Analytical Procedures

2.3.1. Chemical analysis of aqueous solutions – Dissolved sulfate was measured by ion chromatography (IC) using a Dionex DX-100 ion chromatography column after samples were centrifuged (12000RPM) and filtered through a 0.02μm membrane filter. Dissolved Fe(II) and Fe(III) were measured using the revised ferrozine method described by Viollier *et al*[41] at a

wavelength of 562nm (limit of detection was 0.4μmol/L) using a Hewlett-Packard Vectra QS 165 spectrophotometer.

2.3.2. X-ray absorption spectroscopy – Conventional solid-phase identification techniques like x-ray diffraction (XRD) are not capable of identifying non-crystalline phases, and the quantification is even more difficult if multiple phases are present. In this study, solid-phase speciation was determined by S-*K*-edge x-ray absorption near-edge structure (XANES) spectroscopy and Fe-*K*-edge XANES and extended x-ray absorption fine structure (EXAFS) spectroscopy at beam line 4-3 (S-*K*-edge) and beam line 4-1 (Fe-*K*-edge), respectively, at the Stanford Synchrotron Radiation Lightsource (SSRL).

For S-*K*-edge XANES analysis, samples were thinly brushed on sulfur-free Kapton® tape mounted on aluminum sample holders inside a glove box (5% H_2:95% N_2 atmosphere), and XANES data were collected under an inert (He) atmosphere at ambient temperature. Samples and reference standards were diluted 2- to 10-fold with boron nitride (BN) to minimize self-absorption effects associated with high S loadings[42]. X-ray energy was varied using a Si(111) monochromator, with energy calibrated continuously in transmission mode to the maximum of the energy position of S *K*-absorption-edge peaks (*1s* to *3p*) of sodium thiosulfate at 2472.02eV. XANES spectra in x-ray fluorescence mode were collected using a 4-element Si-Li Vortex detector. A minimum of 7-10 spectra was collected for each sample to extract workable average spectra.

For Fe-*K*-edge XANES/EXAFS analysis, a known weight of each sample was diluted with oven-dried boron nitride (BN) powder and pressed into pellets inside a glove box. These pellets were then mounted on aluminum sample holders supported with Kapton® tape. Energy was calibrated at 7111eV, the energy position of the first inflection point in the *K*-edge of an Fe metal foil recorded in double transmission setup. XAS data were collected under a He atmosphere at ambient temperature in a specially designed gas flow chamber in fluorescence mode using a Si(220) double-crystal monochromator and a thirty-element Ge-detector. A

minimum of 7-10 spectra were collected for each sample to obtain a better signal to noise average spectrum for further analysis.

Athena software[43] was used for XANES and EXAFS background subtraction and normalization. The energy position of the absorption-edge feature of S-*K*-edge XANES spectra is expected to constitute a chemical ruler for oxidation state of S species[44]. However, owing to the similarity in XANES spectra for the various model compounds for each oxidation state[45], S *K*-edge XANES spectra were first analyzed by principal component analysis (PCA)[46] using the SIXPACK code[47], in order to estimate the minimum number of components necessary to fit these XANES spectra[48]. Then, target transformation (TT) was used to determine the relevant model compound spectra to be considered as legitimate components (**Table S1, S2**). Details of the PCA-TT procedure are reported in the SI. Finally, quantitative sulfur speciation was determined by linear combination-least squares (LC-LS) fitting of XANES spectra with contributions from selected S reference compounds chosen by the PCA-TT procedure (**Figure S2 and S3**) using the Athena program[45,49]. The quality of the LC-LS fits was estimated by an R-factor parameter (*Rf*) of the following form: $Rf = \Sigma\ (\chi_{exp} - \chi_{calc})^2\ /\ \Sigma\ (\chi_{exp})^2$. The accuracy of the XANES fitting procedure is estimated to be ±10% of the fit-determined component phases[42]. The components below 10% are thus considered as not significant. However, the same model compounds for the LC-LS fitting of the S-*K*-edge XANES spectra were used for all the samples studied; thus, we assume that the occurrence of components comprising less than 10% of the total components as legitimate components if these S species are indicated by the occurrence of its main edge (due to 1s-4p electronic transitions). S-*K*-edge XANES spectra were analyzed by LC-LS fitting (model compounds used for the LC-LS fitting analysis are reported in **Figure S3 (SI)** and shell-by-shell fits, respectively. Shell-by-shell fitting was performed with the program Artemis using the FEFF8 code 8.4[50]. Backscattering phase and amplitude functions were calculated using the FEFF8.4 program for Fe-S and Fe-O pairs.

2.3.3. X-ray diffraction analysis – Synchrotron x-ray powder diffraction data were collected for reacted samples, and redox integrity was maintained by avoiding long x-ray exposures, which was made possible by the much higher flux of a synchrotron x-ray source. An x-ray exposure of 60 seconds was enough to generate an x-ray diffractogram for these samples. A thin film of sample (<1mm) was pasted on Kapton® tape for x-ray diffraction at SSRL beamline 11-3 in transmission geometry using a Mar 345 image plate detector. An x-ray wavelength of 0.976Å (corresponding to an energy of about 12KeV) was employed after calibration using a lanthanum hexa-boride (LaB_6) reference compound. A blank (*i.e.* without sample) with the same Kapton® tape was also analyzed to subtract the Kapton® signals for background corrections, and crystal structure standards sensitive to oxidation were analyzed with the same setups as controls. Data were collected from q = 1.0 to 12.5Å^{-1} with 0.02Å^{-1} step size. Mineral phases were identified using the PDF-2 database

2.3.4 Transmission Electron Microscopy – TEM images were acquired using a FEI Tecnai G2 F20 X-Twin (operating voltage of 200 kV) equipped with a field-emission gun, an x-ray detector (EDS) for compositional analysis, and a CCD camera; the point-to-point resolution was 2.5 Å. Dilute suspensions (prepared using O_2-free milliQ water) of nanoparticles were deposited on ultra-thin holey carbon TEM grids and were dried under a nitrogen (97% N_2 + 3% H_2) atmosphere before TEM observations.

3. Results

3.1 Fe-dissolution and sulfide oxidation in aqueous solution – Bar graphs of Fe dissolution at different sulfide-to-iron (S/Fe) ratios for the three Fe(III)-(oxyhydr)oxides (**Figure 1**) show that the concentration of Fe(II) in solution increased with increased S/Fe ratio up to 0.5 during the sulfidation of all three Fe(III)-(oxyhydr)oxides. However, above S/Fe = 0.5, the concentration of Fe(II) dropped significantly in all solution samples. Iron dissolution for ferrihydrite (124μmol) is

an order of magnitude higher relative to hematite (3μmol) and two orders of magnitude higher relative to goethite (0.5μmol) at a S/Fe ratio of 0.5 (**Figure 1**). Order-of-magnitude differences in surface area-normalized Fe(II) concentrations in solution (**Figure 1B**) and Fe-dissolution rates (**Figure 1C**) suggest that the differences in Fe(II) concentrations in solution are not only controlled by the surface area but also by the chemical and physical properties of the nanoparticle surfaces.

This observation is consistent with the fact that ferrihydrite is poorly crystalline[51,52], has smaller particle size (~5nm), and has higher surface area (~332m^2g^{-1}) compared to hematite (50nm; 32m^2g^{-1}) and goethite (50-70nm, 36m^2g^{-1}). **Figure 1B** shows Fe-dissolution rates for all three Fe(III)-(oxyhydr)oxides at S/Fe ratios up to 0.5; above this ratio FeS precipitation is dominant. Iron dissolution rates (**R (mol.m^2.day^{-1})**) of Fe(III)-(oxyhydr)oxides based on a first-order rate law were calculated as

$$R = \frac{d[Fe^{2+}{}_{aq}]}{\mathrm{A}\ dt}$$

where, A is the surface area concentration of Fe(III)-(oxyhydr)oxides in m^2L^{-1}, and *t* is the time.

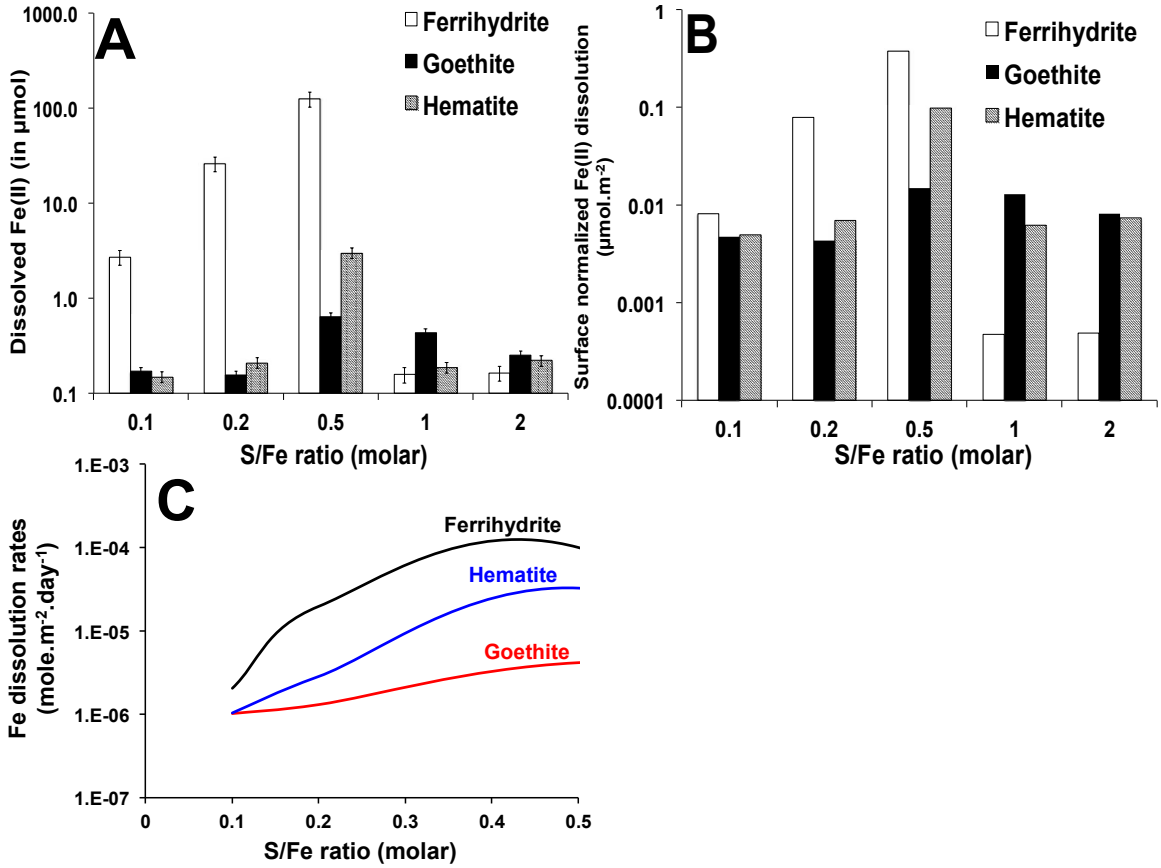

Figure 1: (A) Fe(II) concentrations measured in solution after one day of reaction of ferrihydrite, goethite, and hematite nanoparticles with dissolved sulfide at different S/Fe ratios; **(B)** Surface area-normalized Fe(II) concentrations; **(C)** Fe-dissolution rates (mole.m^{-2}.day^{-1}) for ferrihydrite, goethite, and hematite nanoparticles at different S/Fe ratio.

In the process of reductive dissolution of Fe(III) to Fe(II), dissolved sulfide also oxidizes, forming intermediate sulfur species and eventually sulfate. Dissolved sulfate concentrations were also measured in aqueous solution for all samples after the sulfidation reaction as shown in **Figure 2.** Sulfate concentrations in solution follow a pattern similar to that of iron dissolution, where sulfate concentrations in solution increased (9-12µmol) for all three Fe(III)-(oxyhydr)oxides upto the S/Fe ratio of 0.5, and at higher ratios (>0.5) decreased sharply (0-2 µmol). However, unlike Fe(II) dissolution, dissolved sulfate concentration in ferrihydrite-containing systems was lower (~9µmol) than that in goethite- and hematite-containing systems (~12µmol) at a S/Fe ratio of 0.5 (**Figure 2; Figure S10**). This finding is consistent with the fact

that higher dissolution rates of Fe(II) in case of ferrihydrite means more Fe(II) is available to react with sulfide before eventual oxidation of sulfide, hence less sulfate in the solution.

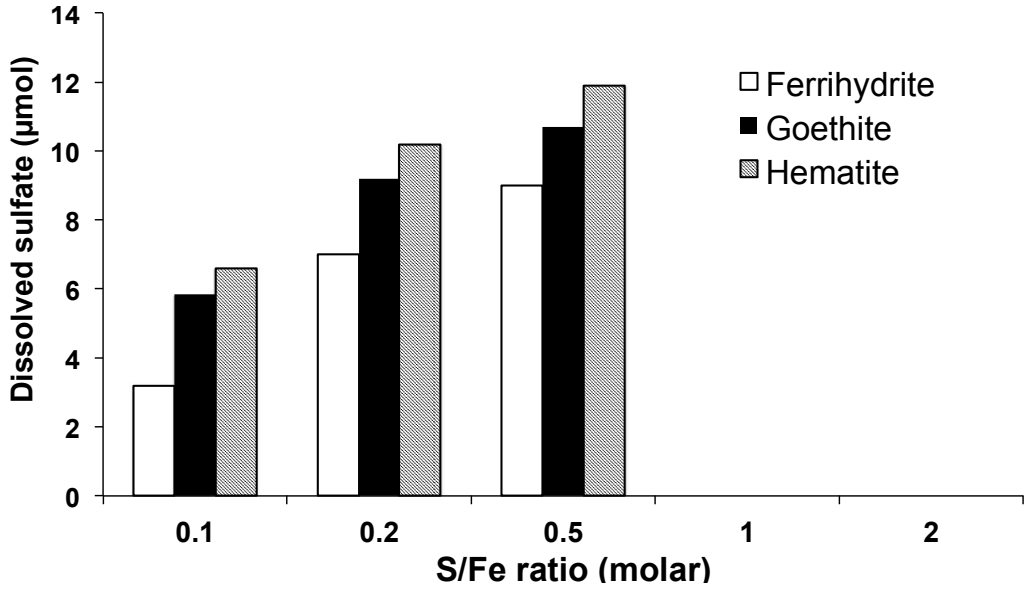

Figure 2: Dissolved sulfate concentration measured after (14 days) sulfidation reactions of ferrihydrite, goethite, and hematite nanoparticles as a function of different S/Fe molar ratios.

3.2 Fe-*K*-edge X-ray Absorption Spectroscopy

The pre-edge regions and the fully normalized Fe *K*-edge XANES spectra obtained from solid samples after 14 days of reaction of different Fe(III)-(oxyhydr)oxides with dissolved sulfide and linear combination fitting results are shown in **Figure 3**. It is well known that the position of the pre-edge features (due to 1*s* to 3*d* electronic transitions) depends on the redox state of Fe in Fe-bearing minerals[53,54]. The number, integrated intensities, and positions of absorption features in the pre-edge region of Fe *K*-edge XANES spectra depend on Fe oxidation state as well as on the symmetry and distortion of the site in which Fe resides. Fe(III) is characterized by a pre-edge feature centered around 7114eV, whereas Fe(II) is characterized by a pre-edge features centered around 7112eV. The pre-edge feature of the XANES spectra collected for ferrihydrite samples is centered around 7114eV, whereas this feature clearly moves toward 7112eV in the presence of dissolved sulfide with increasing of S/Fe ratio (**Figure 3**). Such an evolution suggests that the redox state of Fe changed from Fe(III) to Fe(II).

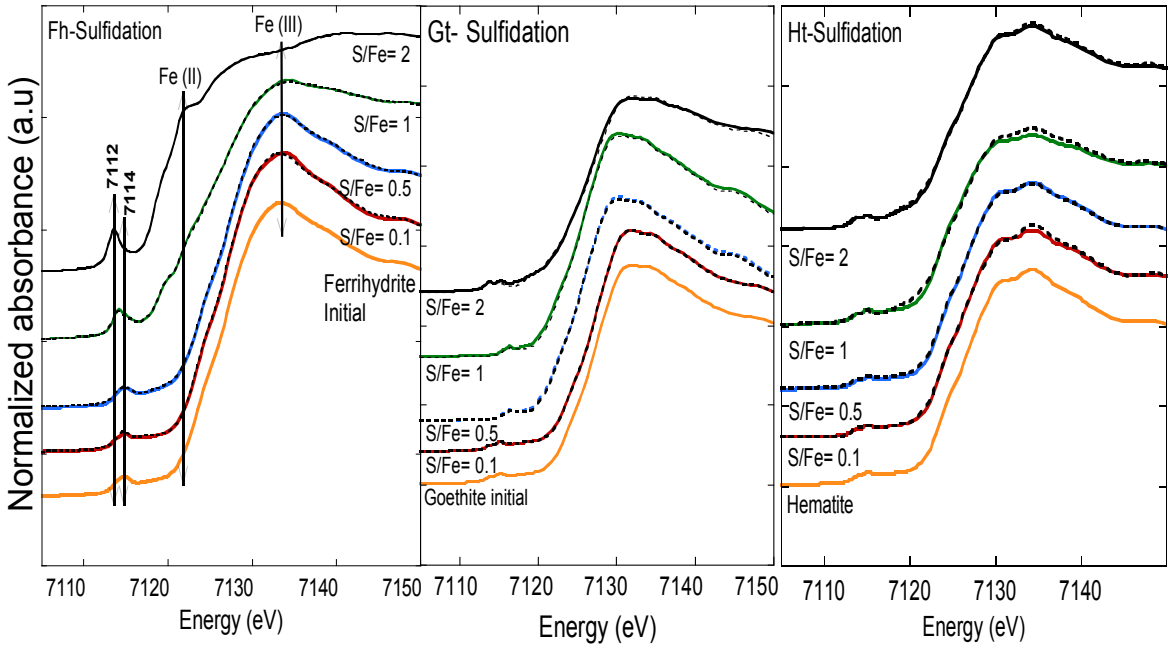

Figure 3: Fe-*K*-edge XANES spectra of ferrihydrite **(Fh)**, goethite **(Gt)**, and hematite **(Ht)** nanoparticles taken after 14 days of reaction with dissolved sulfide at different S/Fe ratios. Dotted lines are linear combination fit results of the XANES region of the sample spectra (solid lines)

These observations are also confirmed by the Fe *K*-edge XANES spectra, which show a decrease in the intensity of the white-line (Fe(III) and the appearance of a shoulder on the low-energy side of this white-line, due to the presence of (Fe(II), with increasing of S/Fe ratio (**Figure 3**). These changes suggest the formation of reduced solid-phase Fe species during the reaction of ferrihydrite nanoparticles with dissolved sulfide. There was no significant change in the energy position or integrated intensity of pre-edge features of the goethite and hematite Fe *K*-edge XANES spectra, suggesting that the majority of Fe remained oxidized under the same reaction conditions (with sulfide), as is the case for the ferrihydrite nanoparticles.

Similar behavior was also observed in the Fe-*K*-edge EXAFS spectra, where changes are evident only in ferrihydrite at S/Fe ratios > 0.5. The Fe-*K*-edge EXAFS spectra and the corresponding Fourier Transform of the normalized, background-subtracted, and k^3-weighted ferrihydrite EXAFS spectrum after reaction with dissolved sulfide are presented in **Figure 4**. The EXAFS spectra show distinctive features which change with increasing S/Fe ratio. These

changes are also observed in the corresponding Fourier Transforms, which show a shift of both the first- and second-neighbor peaks from 1.4Å and □2.7Å (uncorrected for phase shift), at a S/Fe ratio of 2. This shift suggests a change in the Fe co-ordination environment and a change of first-neighbor atoms around Fe in the structure. More specifically, the Fe-*K*-edge XANES and EXAFS of end-member ferrihydrite in the presence of HS^- compare well with those of mackinawite produced from reduction of dissolved Fe(III)[55] suggesting formation of FeS species.

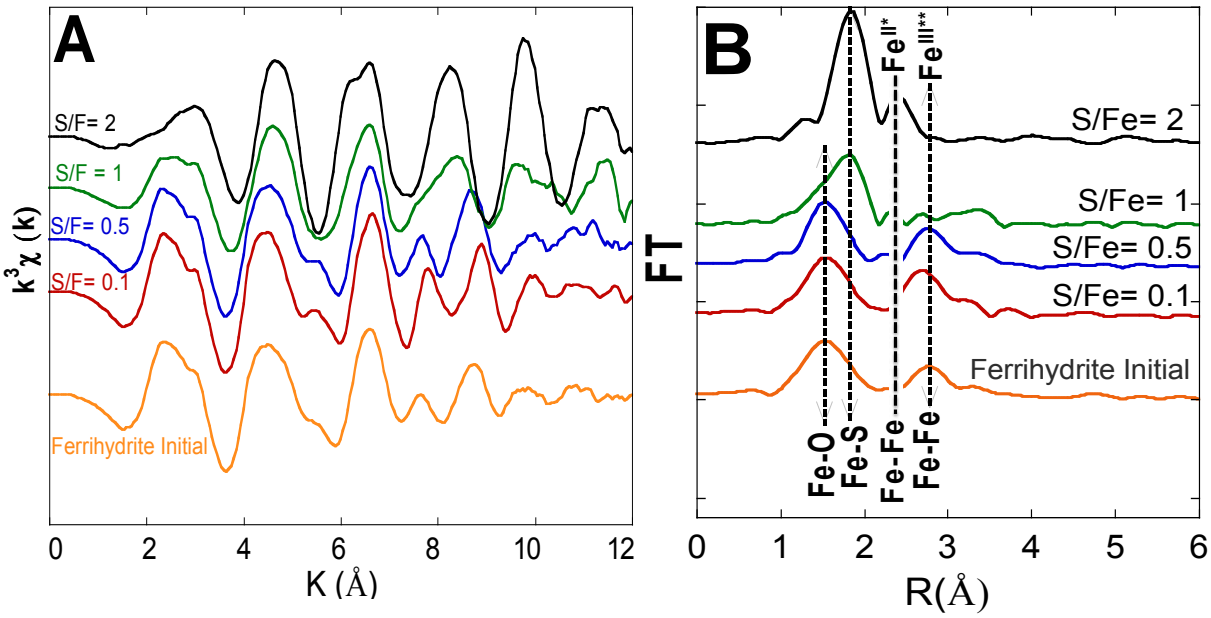

Figure 4: (A) Background-subtracted and k^3-weighted Fe-*K*-edge EXAFS spectra of ferrihydrite at different S/Fe ratios; **(B)** Fourier Transform Magnitudes of the EXAFS spectra of ferrihydrite nanoparticles after 14 days of reaction with dissolved sulfide at different S/Fe ratios. $^{*}Fe^{II}$-Fe^{II} and $^{**}Fe^{III}$-Fe^{III} shells were calculated with the FEFF 8.1 code using the crystal structure of mackinawite[56] and ferrihydrite[51], respectively.

3.3 S-*K*-edge XANES Spectroscopy

Following the sulfidation reactions, solid-phase samples were analyzed by sulfur K-edge XANES spectroscopy to determine sulfur transformations and the types of intermediate sulfur species formed during the reaction. **Figure 5** shows S-*K*-edge XANES spectra of different sulfur

species identified at different S/Fe ratios for the different Fe(III)-(oxyhydr)oxide nanoparticles after 14 days of reaction.

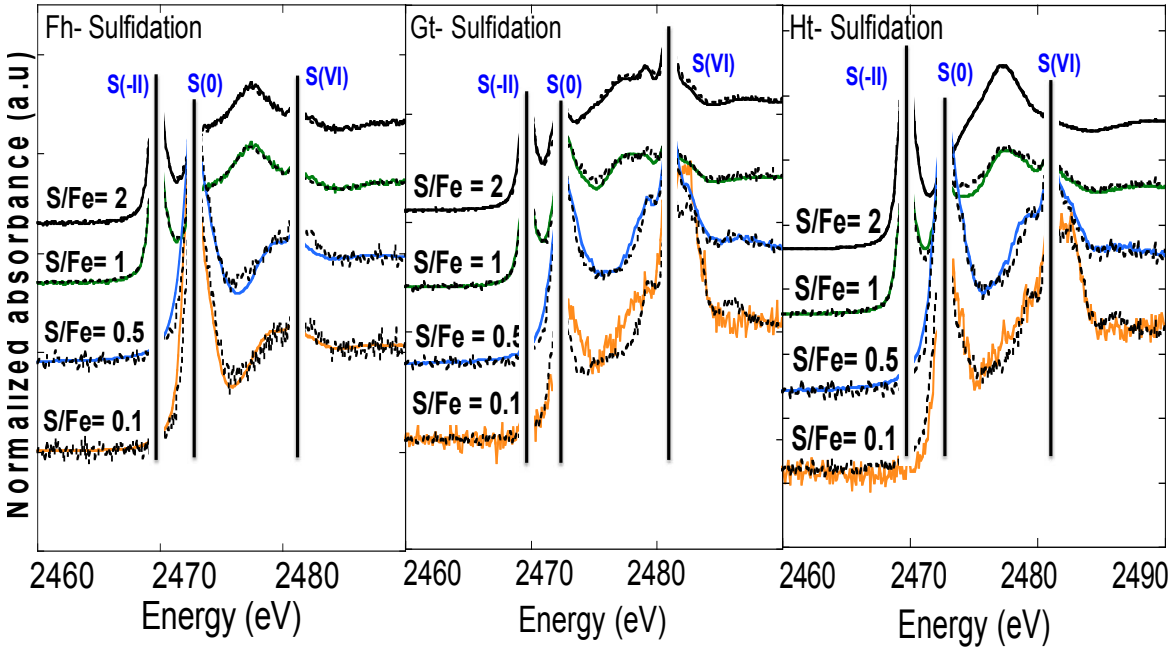

Figure 5: S-*K*-edge XANES spectra of ferrihydrite, goethite, and hematite nanoparticles after 14 days of reaction with dissolved sulfide at different S/Fe ratios.

The energy positions of absorption-edge peaks of the S *K*-edge XANES spectra (due to 1s to 3p electronic transitions) decreased from 2472 eV, characteristic of S(0), to 2469.4 eV, characteristic of S(-II), when the S/Fe ratio was > 0.5. This observation suggests formation of Fe-monosulfides. However, S(-I), characteristic of disulfides like pyrite and having typical *K*-edge energy positions of 2471eV[44] was not detected in our samples. There is also a clear signal for S(VI), characteristic of sulfate species, which have a *K*-edge energy of 2482eV. The highest peak intensity of sulfate is observed at low S/Fe ratios and gradually decreases as S/Fe ratio increases (**Figure 5**) in goethite and hematite. Interestingly, the sulfate peak was absent or less abundant in the case of ferrihydrite, suggesting a faster and more complete sulfidation reaction without further oxidation of sulfide.

3.4 EXAFS Spectroscopic Analysis of Ferrihydrite After Sulfidation

Our XAS observations suggest that ferrihydrite is totally dissolved at the end of the sulfidation reaction (14 days), and was replaced by a reaction product that is similar to an iron sulfide like mackinawite. To identify this reaction product, shell-by-shell fitting was performed for the EXAFS spectrum of ferrihydrite at a S/Fe ratio of 2 (**Figure 6**).

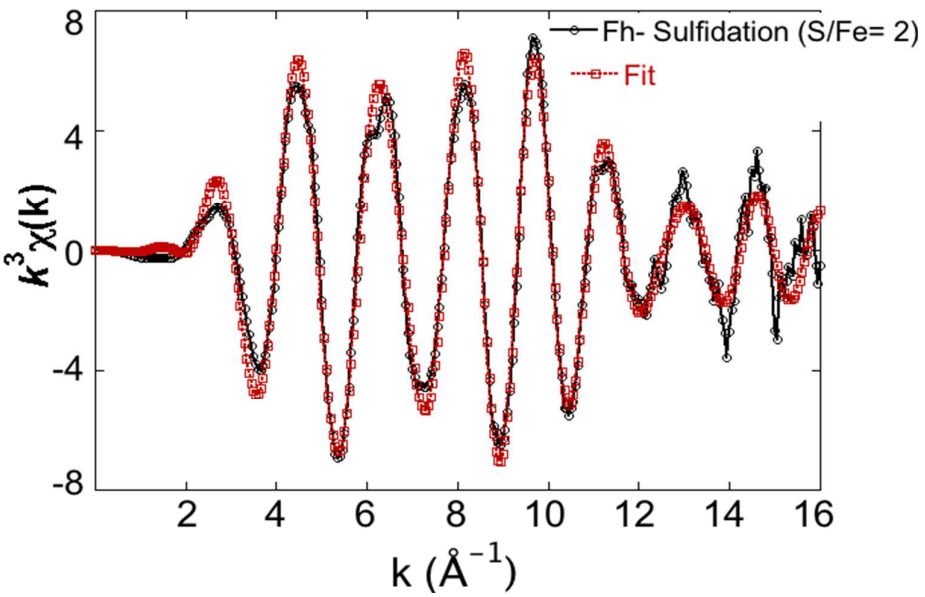

	Fe-S	Fe-Fe
N	3.4 ± 0.1	1.0 ± 0.2
D(Å)	2.23(1)	2.72(1)
σ^2(Å^2)	0.0041(4)	0.0042(15)
ΔE_0 (eV)	1.1±0.1	
R^2	0.0058	
χ^2	3.76.83	

Figure 6: Shell-by-shell fits of EXAFS spectra of ferrihydrite after reaction with dissolved sulfide at a S/Fe ratio of 2 after 14 days. Fitting range R = 1-3.5Å, Fourier transform range: k = 3.4-14.8Å^{-1}; Number of independent data points N_{ind} = 18, Number of variables = 7.

This spectrum was selected for shell-by-shell fitting because it showed total conversion; thus, it was also used as a reference for FeS for the LC-LS fittings of the other spectra. The best fit indicates that the interatomic distance between Fe and S is 2.23 (± 0.01)Å and the Fe-Fe

distance is 2.74 (± 0.01)Å. The FEFF path for the Fe-O pair did not give satisfactory fits for the experimental spectra. The distance of 2.23Å is typical of mackinawite produced from reduction of Fe(III)[55], which is referred to as minimally oxidized mackinawite[45].

4. Discussion

4.1 Influence of Sulfide-to-Iron (S/Fe) Ratios on Sulfidation Mechanisms

Our sulfidation studies of Fe(III)-(oxyhydr)oxide nanoparticles clearly show that S/Fe ratio is very important in determining the types of sulfidation mechanisms. **Figure 7** shows the distribution of mass percentages of FeS and Fe(III)-(oxyhydr)oxide species in the solid-phase sample after 14 days of the sulfidation reaction as a function of S/Fe molar ratio. These results suggest that reductive dissolution of Fe(III)-(oxyhydr)oxides precedes the precipitation of FeS species only for S/Fe ratios > 0.5. At lower S/Fe ratios (≤ 0.5), this reductive dissolution results in Fe(II) release into aqueous solution, but it does not drive FeS precipitation. High concentrations of sulfide (S/Fe ratios ≥0.5) are needed to react further with Fe(II), derived from reductive dissolution of Fe(III)-(oxyhydr)oxides to precipitate FeS (**Figure 5**). Such precipitation removes Fe(II) from solution as suggested by the decreasing amount of dissolved Fe and sulfate (**Figures 1** and **2**). A sudden drop in Fe(II) concentration and no precipitation of FeS at S/Fe ratios lower than 0.5 suggest that some degree of super-saturation is required for FeS precipitation. The Fe(II) concentrations in solution were an order of magnitude different for different Fe(III)-(oxyhydr)oxides and still required similar sulfide concentrations in solution to precipitate FeS, indicating sulfide concentration controls FeS precipitation as previously suggested[57]. Finally, S/Fe ratios > 0.5 are required for spontaneous nucleation of FeS, and the production rate of FeS is directly proportional to the increase in sulfide concentration (**Figure 7**). Thus, these results suggest that the ratio of dissolved sulfide to Fe has a major influence on Fe(II) dissolution and FeS precipitation in low-temperature experimental sulfide systems. However, in natural systems or in the presence of other metal ions, this ratio could be higher as

some metal monosulfides have lower solubility products (Hg<Cu<Cd<Sn≈Pb<Ni<Fe)[58] than Fe-monosulfide and could precede FeS precipitation using dissolved sulfide.

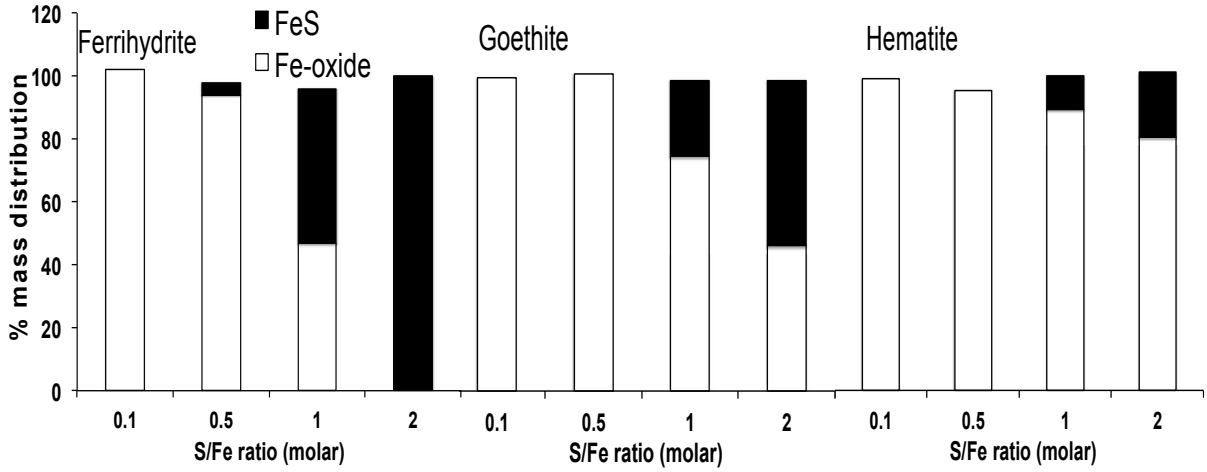

Figure 7: Mass percentage of Fe(III)-(oxyhyrdr)oxides and FeS in solid-phase samples after 14 days of the sulfidation reaction as determined by linear combination fits of the Fe-*K*-edge XANES spectra. Fe species are expressed as the relative proportion of each of the Fe model compounds normalized to 100%.

4.2 Impact of Crystallinity and Surface Area on Sulfidation of Fe(III)-(oxyhydr)oxide

It is well established that ferrihydrite, goethite, and hematite nanoparticles have different atomic-level structures and morphologies. Comparison of the surface area-normalized Fe-dissolution rates of each Fe(III)-(oxyhydr)oxide (**Figure 1C**) clearly shows that ferrihydrite nanoparticles, with orders of magnitude higher dissolution rates, will produce an order of magnitude higher dissolved Fe(II) in solution than hematite nanoparticles and two orders of magnitude higher dissolved Fe(II) in solution than goethite nanoparticles. However, the goethite nanoparticles, which have a slightly higher surface area (36 $m^2.g^{-1}$) per gram than hematite (32 $m^2.g^{-1}$) nanoparticles, produced lower dissolved Fe(II) in solution at similar S/Fe ratios due to lower dissolution rates. This result is consistent with previous field observations on red tropical soils[59], where hematite dissolution rate was found to be an order of magnitude higher than that of goethite. Based on these observations, we conclude that the production of dissolved Fe(II) is controlled not only by surface area but also by the surface properties of Fe(III)-(oxyhydr)oxide,

particularly the atomic-level structures of the three nanoparticle surfaces in contact with aqueous solution. This suggestion is in agreement with previous studies, which found that surface area alone does not control reductive dissolution of Fe(III)-(oxyhydr)oxides by dissolved sulfide, but rather that the dissolution behavior also depends on atomic-level surface properties of these hydrated nanoparticles[32,60]. The (0001) surface of hydrated bulk hematite has oxygen atoms that are singly coordinated by octahedral Fe(III) ions, and thus are likely to have greater proton lability and will be more reactive[61] than the (100) surface of hydrated bulk goethite, where surface oxygens are bonded to two Fe(III) ions[62]. Very little is known about the surface structures of ferrihydrite, goethite, or hematite nanoparticles in contact with aqueous solutions. The above discussion of differences in the structures of hydrated single-crystal hematite (0001) and hydrated single-crystal goethite (100) surfaces is included only to point out potential differences between the structures of these two surfaces, which may or may not be relevant to hematite and goethite nanoparticle surfaces in the environment.

At higher sulfidation rates (S/Fe ratios > 0.5), spontaneous nucleation of FeS occurs, with ferrihydrite showing the highest mass of FeS formed during the sulfidation reaction, followed by goethite and hematite (**Figure 7**). Ferrihydrite was entirely transformed to FeS at an S/Fe ratio of 2 in our experiments, whereas in the cases of goethite and hematite, a maximum of 58% and 18% of these phases, respectively, was transformed to FeS at an S/Fe ratio of 2. In contrast with goethite and hematite, ferrihydrite is a poorly ordered Fe(III)-(oxyhydr)oxide, and thus is likely to have more undersaturated bonding of surface oxygens and hydroxyls than goethite or hematite surfaces. As a result, ferrihydrite should be more sensitive to reductive dissolution, as previously observed in field studies[36,45,63] and as observed in the present study. So, it is likely that degree of crystallinity and attendant differences in atomic-level surface structures, influence the rate of conversion from Fe(III)-(oxyhydr)oxide to FeS. It is also important to note that the aggregation behavior of these nanoparticles might be different once in suspension and that the surface area measured by BET (dry powder) in this case might not be truly representative of the surface areas

of natural Fe(III)-(oxyhydr)oxide nanoparticles. However, currently, we do not have an analytical method available that can reliably measure the surface area of nanoparticles in suspension.

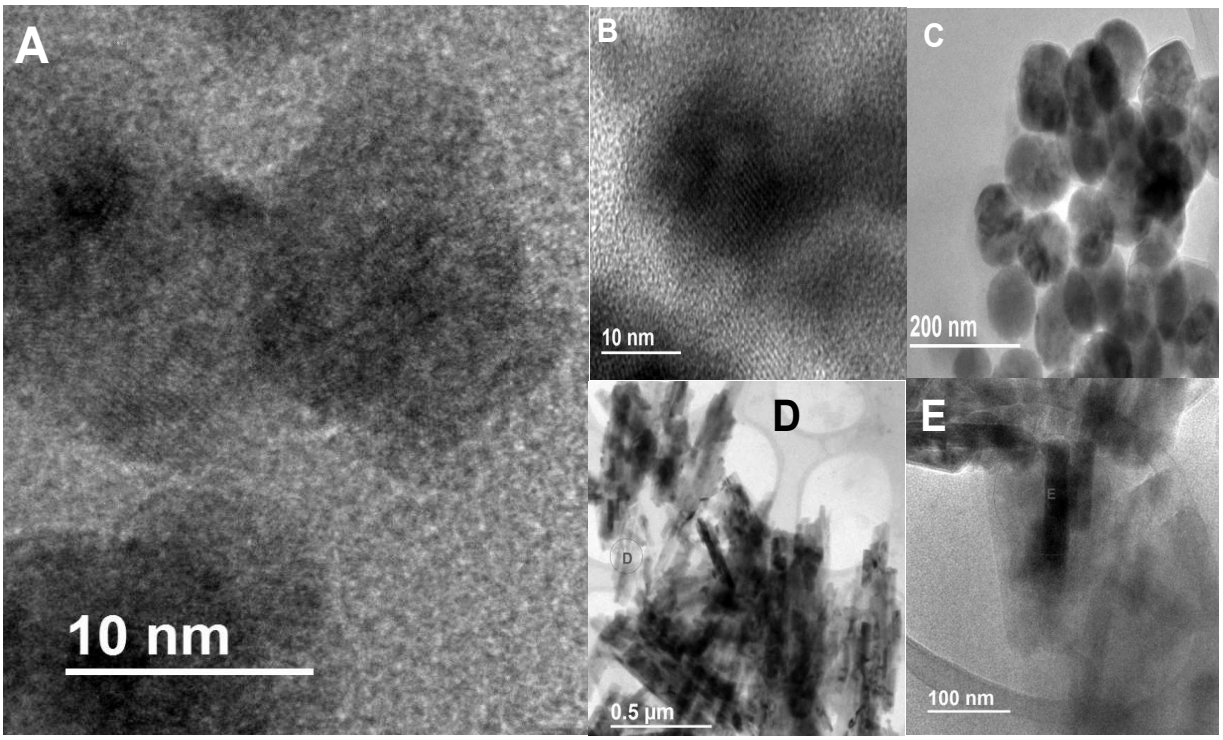

Figure 8: TEM images of (A) ferrihydrite (S/Fe = 0.5), (B) ferrihydrite (S/Fe = 2), (C) hematite (S/Fe = 2), (D) and (E) goethite (S/Fe = 2) nanoparticles.

TEM analysis of sulfidized Fe(III)-(oxyhydr)oxide nanoparticles suggests that FeS precipitated as a separate phase. We did not observe core-shell structure formation in these nanoparticles after reaction with dissolved sulfide, in contrast with study of silver nanoparticle sulfidation where a core-shell structure was observed[64]. We also did not observe a close spatial association of the FeS nanoparticles with the sulfidized Fe(III)-(oxyhydr)oxide nanoparticles as was found for sulfidation of ZnO nanoparticles, where a porous shell of 2.5 to 5 nm ZnS nanoparticles surrounded the ZnO nanoparticles[65]. Our TEM observations suggest that the FeS phases precipitated using dissolved Fe(II) released from reductive dissolution of Fe(III)-(oxyhydr)oxides and dissolved sulfide. Also, as the mechanism of sulfidation seems to be similar

in the three types of Fe(III)-(oxyhydr)oxide nanoparticles studied here, it is reasonable to assume that surface structure of the different Fe(III)-(oxyhydr)oxide nanoparticles is the primary control on reductive dissolution of Fe(III) and release of Fe(II) to the solution and FeS precipitation thereafter is independent of the nature of initial Fe(III)-(oxyhydr)oxide used.

4.3 Formation of Intermediate Sulfur Species During Sulfidation of Fe(III)-(oxyhydr)oxides

Sulfur is characteristically hetero-valent, exhibiting a large range in oxidation state (-II to +VI). Thus, it is imperative to identify and quantify all of the species formed during the reaction of Fe(III)-(oxyhydr)oxide nanoparticles with dissolved sulfide.

Principle component analysis indicates that 99% of the total variance of the system of our 24 XANES spectra (from all three Fe(III)-(oxyhydr)oxide nanoparticles before and after sulfidation) can be explained by the three first principal components[48] (**Table S3, S4**), with a minimum IND parameter value of $7.98 \cdot 10^{-6}$. However, adding the fourth principal component improves the variance and the quality of reconstruction of the whole set of experimental XANES spectroscopic data. Among our large set of model compound spectra, the Target Transform (TT) analysis helped in selecting the most appropriate model reference compounds for the LC-LS fits of the S-*K*-edge XANES spectra of experimental samples (**Table S2**). The model compounds yielding a Normalized Sum of Squared Residuals ($R_{TT} = \Sigma (k^3\chi_{exp} - k^3\chi_{model})^2 / \Sigma (k^3\chi_{model})^2$) lower than 0.15 and SPOIL values below 6 after the TT procedure were considered as possible components[66,67]. Among all tested model compounds, elemental sulfur, minimally oxidized mackinawite, polysulfides, thiosulfate, and jarosite yielded the lowest R_{TT} and SPOIL values. This result suggests that these five S-containing species are likely to represent S speciation in the 24 samples we studied using S-*K*-edge XANES spectroscopy. The high SPOIL values combined with the higher R_{TT} values of greigite, pyrite, Na sulfite, marcassite, pyrrothite, troilite, arcanite, Na-sulfate, malenterite, rhomboclase, K_2SO_4, anhydrite, and quenstedtite indicated that these S-containing species were not present at detectable concentrations in our experimental samples.

The S-*K*-edge XANES spectra of iron sulfides produced during reductive dissolution of ferrihydrite exhibit a peak at 2470eV, which was previously interpreted as precipitation of greigite from reductive dissolution of Fe(III)-(oxyhydr)oxides in a tidally re-flooded wetland[20]. However, in subsequent studies[45,68], it was found that synthetic FeS exposed to sub-stoichiometric amounts of oxidants or Fe(III), referred to as minimally oxidized mackinawite, exhibits a peak at 2470.3eV. The S-*K*-edge XANES peak at 2470eV, characteristic of S(-II), could thus be interpreted as partially oxidized mackinawite. This conclusion corroborates the results of shell-by-shell fitting of Fe-*K*-edge EXAFS spectra.

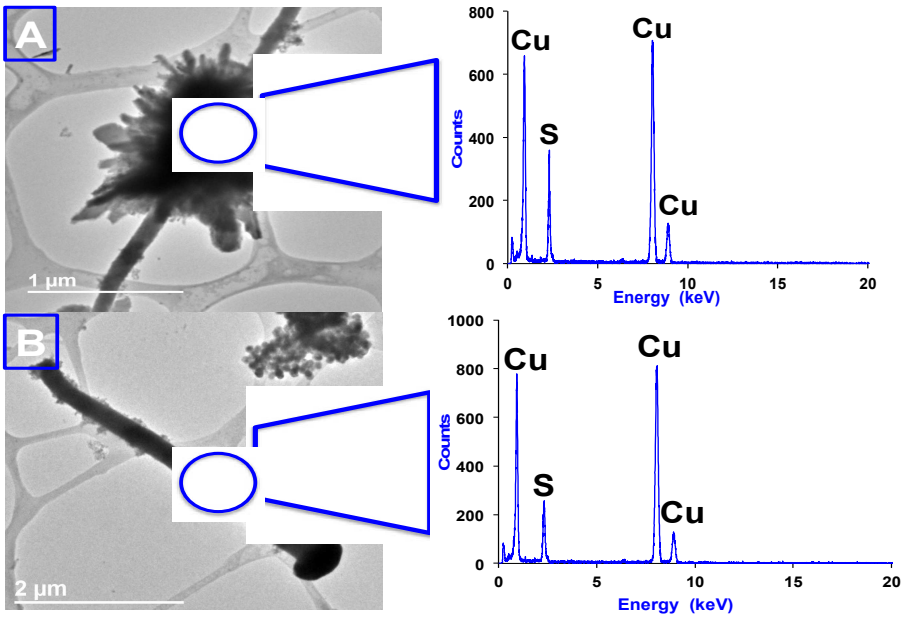

Figure 9: TEM image from sulfidated hematite nanoparticles (A) precipitates (B)"nanonails" showing solid phase sulfur in rod shaped formation.

LC-LS fitting of the S-*K*-edge XANES spectra shows that different types of sulfur species formed at different S/Fe ratios during sulfidation of the three types of Fe(III)-(oxyhydr)oxide nanoparticles (**Figure 10**). At S/Fe ratios ≤ 0.5, S(0) and polysulfides are the main solid-phase species. In the sulfidized goethite and hematite samples, thiosulfate and Fe(II)-sulfate were also observed. TEM analysis showed solid phase sulfur species in sulfidated hematite samples (**Figure 9**). However, these species were not detected in the sulfidized ferrihydrite samples, perhaps due to faster and more complete reaction of the ferrihydrite with

dissolved S(-II). The FeS fraction determined here is consistent with the results from Fe-*K*-edge XANES spectroscopy.

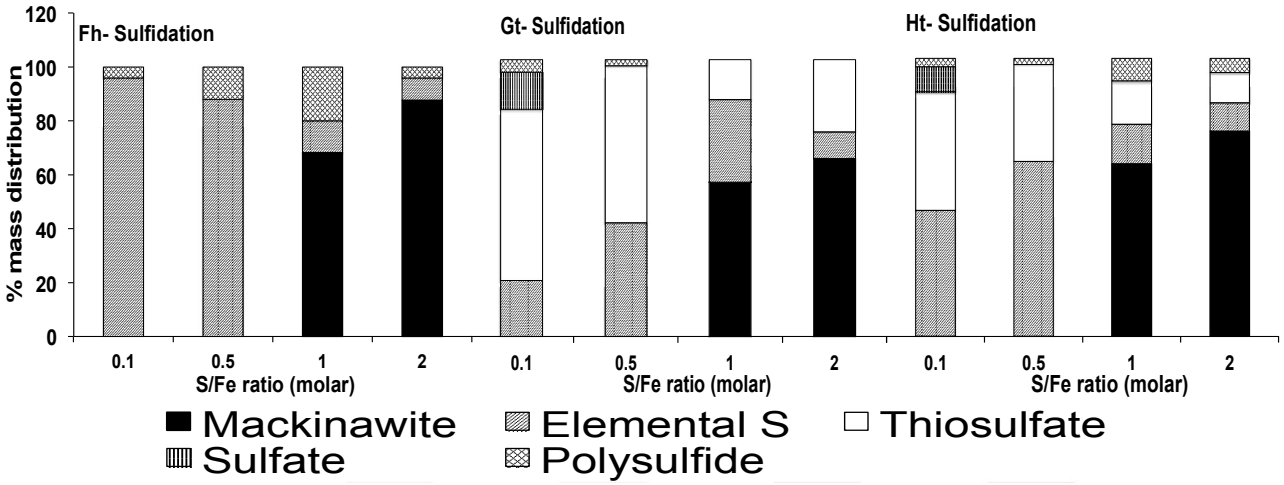

Figure 10: Sulfur species identified in solid phase after 14 days of reaction between ferrihydrite (Fh), goethite (Gt), and hematite (Ht) nanoparticles and dissolved sulfide, Mass percentages of these species were derived from linear combination fitting of S-*K*-edge XANES spectra of samples and selected reference compounds.

Oxidation of S(-II) to SO_4^{2-} is kinetically favored in the presence of oxygen. Sulfite, once formed, does not contribute to further reactions with Fe but reacts rapidly with H_2S, resulting in the formation of thiosulfate[25], which helps explain the presence of thiosulfate in our experiments. At S/Fe ratios ≤ 0.5, sulfide is oxidized (in the process of reducing Fe(III) to Fe(II)), first to elemental sulfur (S(0)) and eventually to sulfate via reactions 1 and 3 below, resulting in the release of Fe(II) into aqueous solution as we observed in our experiments (**Figure 1**).

$$Fe^{3+} + S^{2-} \rightarrow Fe^{2+} + S^0 + e^- \quad (1)$$

$$Fe^{2+} + S^{2-} \rightarrow FeS_{(m)} \quad (2)$$

$$S^0 + 6Fe^{3+} + 4H_2O \rightarrow SO_4^{2-} + 6Fe^{2+} + 8H^+ \quad (3)$$

$$S_2O_3^{2-} + 8\,Fe^{3+} + 5H_2O \rightarrow \square\square\square\square^{\square\square} + 8\,Fe^{2+} + 10\,H^+ \quad (4)$$

$$Fe^{2+} + SO_4^{2-} \rightarrow FeSO_4 \quad (5)$$

$$S^0 + HS^- \Leftrightarrow S_2^{2-} + H^+ \quad (6)$$

$$S_2^{2-} + S_2^{2-} \rightarrow S_4^{2-} + 2e^- \quad (7)$$

$$S^{2-}_{n-1} + S^0 \rightarrow S^{2-}_n \quad (8)$$

The higher Fe-dissolution rates of ferrihydrite relative to goethite and hematite, contribute to the higher release of Fe(II) into solution and greater production of S(0) in the solid phase during the sulfidation reaction of ferrihydrite nanoparticles. Additionally, higher Fe-dissolution rates of ferrihydrite nanoparticles provided a continuous supply of dissolved Fe(II) in solution to react rapidly with available dissolved sulfide at higher S/Fe ratios causing the precipitation of FeS (reaction 2). In contrast, the Fe-dissolution rates of Fe(II) from goethite and hematite nanoparticles were much lower than for ferrihydrite, so the initially formed S(0) is suspected to result in the formation of polysulfide *via* a disulfide route (reactions 6 and 7). Disulfides are end members of a series of sulfanes, usually referred to as polysulfides, which occur as discrete species in aqueous solution[69]. However, they have not been commonly identified in these systems. Nonetheless, they play an important role in the reactions of Fe with sulfide. Rickard[27] proposed the polysulfide pathway for the formation of pyrite involving the dissolution of FeS followed by the reaction of Fe(II) and sulfur species forming pyrite (reactions 9 and 10)

$$FeS + S_n^{2-} = FeS_2 + S_{(n-1)}^{2-} \quad (9)$$

$$FeS + H_2S = FeS_2 + H_2 \quad (10)$$

Wang and Morse[39] suggested that S(0) is a key reactant in the formation of pyrite, which also includes the dissolution of FeS. However, Schoonen[70] concluded that elemental sulfur is not the true reactant in the formation of pyrite and agreed with previous studies suggesting that the hydrolysis of sulfur or reaction of S(0) with H_2S creates polysulfide species, which are more likely to be the reactants[29,38].

We also detected solid-phase polysulfide species after the reaction of Fe(III)-(oxyhydr)oxides with dissolved sulfide resulting from eventual oxidation and precipitation of dissolved sulfide. During this reaction, sulfate is also present in aqueous solution as observed in **Figure 2**. At higher S/Fe ratios (> 0.5) where sulfate decreased to undetectable levels, formation

of FeS reaches a maximum. Once the available Fe(II) is converted to FeS, the H_2S concentration builds up in the system with increasing S/Fe ratio, and Fe dissolution is no longer viable or occurs at an extremely slow rate. Also, in the sulfidation reactions of goethite and hematite, the likely formation of surface precipitates of sulfur species may result in slow electron transfer (**Figure 10**) limiting Fe(II) dissolution. Although H_2S is not a good electron donor because the highest occupied molecular orbital is so stable, it can still act as an electron donor to Fe(II) because Fe(II) has an unoccupied low-energy atomic orbital. As a result, Fe-dissolution continues, but very slowly. Also, because Fe-dissolution is slow in the sulfidation reaction of hematite, we observed thiosulfate even at the highest S/Fe ratios (S/Fe =2). However, this is not the case in the sulfidation reaction of ferrihydrite nanoparticles, where Fe dissolution and FeS formation are complete. **Figure 11** shows schematically the pathways of these reactions for different S/Fe ratios.

The adsorption of dissolved sulfide to Fe(III)-(oxyhydr)oxide nanoparticle surfaces occurs rapidly due to the formation of inner-sphere complexes $>FeS^-$ as suggested previously[71]. Electrons are transferred at the nanoparticle surfaces between the initially formed inner-sphere complexes and the Fe(III) in the nanoparticles[72]. During reductive dissolution of Fe(III)-(oxyhydr)oxides by dissolved sulfide, a large portion of the reduced iron remains at the Fe(III)-(oxyhydr)oxide nanoparticle surfaces or is bound to the solid phase due to the formation of FeS and mixed-valent iron oxides[32,73,74]. In the presence of sulfate, reductive dissolution of Fe(III)-(oxyhydr)oxides is inhibited and reaction rates are usually lower than in the absence of sulfate[75]. These observations explain the decrease in Fe(II) concentrations in solution during the reaction of goethite and hematite after sulfate precipitation at higher S/Fe rations (> 0.5).

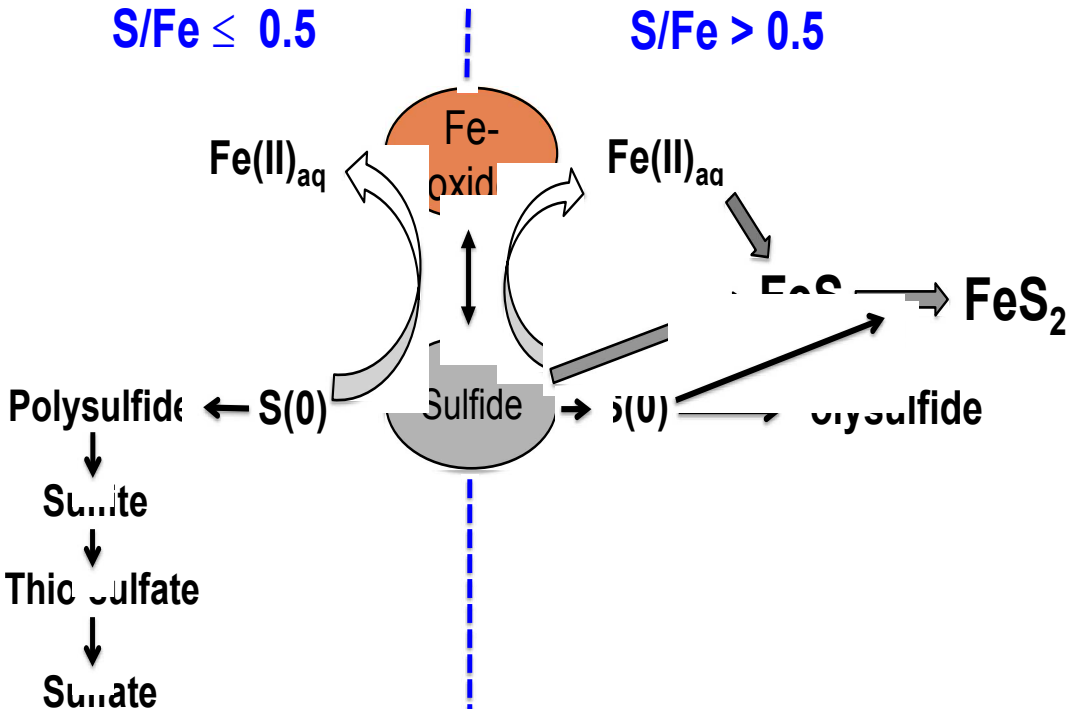

Figure 11: A schematic representation of the reaction pathways of sulfidation of Fe(III)-(oxyhydr)oxides at different S/Fe ratios.

5. Conclusions and Environmental Implications

Iron sulfides are an intrinsic and essential part of the global biogeochemical cycles of sulfur and iron[25]. Understanding their formation and subsequent transformations is essential for understanding the mobility and sequestration of heavy metal contaminants associated with iron sulfides[13,14,18,55,76,78-80]. Our experimental results provide a mechanistic understanding of the formation of FeS as well as intermediate sulfur species from the reductive dissolution of Fe(III)-(oxyhydr)oxide nanoparticles in the presence of dissolved sulfide. They also indicate that the S/Fe ratio is critical in determining Fe(II) concentrations in solutions and the potential for FeS precipitation. A S/Fe ratio > 0.5 is required to precipitate FeS. Our results also show that the surface areas of the Fe(III)-(oxyhydr)oxide nanoparticles examined exert a major control on reductive Fe-dissolution in the presence of sulfide; however, Fe-dissolution rates normalized to surface area suggest order-of-magnitude differences for different Fe(III)-(oxyhydr)oxide, indicating that surface structure and other surface properties of these nanoparticles are likely

important. However, our study was conducted on highly simplified systems. Natural environmental systems should exhibit more complexity in terms of competing ions, ionic strength variations, presence of organic matter, *etc*.

The environmental impacts of these processes are vast, as Fe(III)-(oxyhydr)oxide nanoparticles exert a major control on the mobility and behavior of contaminants in waters and soils. Also, reduction of Fe(III)-(oxyhydr)oxides in subsurface environments plays an important role in electron cycling in water-sediment systems. Redox transformations in these environments are frequent, and microbial sulfate-reduction is ubiquitous. These redox changes will stimulate sulfidation of Fe(III)-(oxyhydr)oxide nanoparticles and eventually lead to the release or result in the co-precipitation of surface-sorbed contaminants, depending on the availability of dissolved sulfide (S/Fe ratio).

An important result of this sulfidation process is the difference in pH_{pzc} of the original Fe(III)-(oxyhydr)oxides *vs*. their sulfidized reaction products. The pH_{pzc} values of Fe-sulfides like mackinawite (pH_{pzc} = 2.9) and pyrite (pH_{pzc} = 2.0-2.4)[81] are much lower than the pH_{pzc} values of Fe(III)-(oxyhydr)oxides like ferrihydrite (pH_{pzc} = 7.9)[82]; goethite (pH_{pzc} = 8.32)[83]; hematite (pH_{pzc} = 7.82)[83]. The lower pH_{pzc} values imply that the particle surface will be highly negatively charged at common environmental solution pH values (such as in our experiments ~7.2 ±0.2), resulting in higher inter-particle repulsion and consequently, lower particle aggregation. This would eventually provide larger surface area and higher sorption efficiency for positively charged metal ions at newly formed Fe-S surfaces. The more negative surface charges of iron sulfide nanoparticles than iron oxide nanoparticles should also result in enhanced adsorption of cation contaminants onto the former.

On a global scale, these processes also have important environmental implications associated with climate change-induced sea level rise and seasonal flooding of rivers. For example, sea level rise would bring sulfate-rich seawater to coastal areas which could potentially alter the biogeochemistry of redox-sensitive elements by turning formerly oxic zones into more

reducing zones, resulting in reductive dissolution of Fe(III)-(oxyhydr)oxides. Such dissolution would release surface-sorbed contaminants to the environment. On the other hand, river water flooding would also create reducing conditions but with lower sulfate concentrations providing a lower S/Fe ratio. Additional studies are needed to better understand these river water and sea water scenarios on the redox cycling of Fe(III)-(oxyhydr)oxides and associated contaminants and to assess the associated risks for humans and environments since almost 25% of the world's population lives in coastal areas.

Acknowledgments: This work was supported by the U.S. National Science Foundation and the U.S. Environmental Protection Agency under NSF Cooperative Agreement EF-0830093, the Center for the Environmental Implication of NanoTechnology (CEINT), based at Duke University. This work has not been subjected to EPA review and no official endorsement should be inferred. The technical staffs at the Stanford Synchrotron Radiation Lightsource, SLAC National Accelerator Laboratory (Menlo Park, California, USA) are thanked for technical support during XAS measurements. SSRL and SLAC are supported by the U.S. Department of Energy, Office of Science, Office of Basic Energy Sciences under Contract No. DE-AC02-76SF00515, the DOE Office of Biological and Environmental Research, and the National Institutes of Health, National Institute of General Medical Sciences (including P41GM103393). The authors also wish to thank Dr. Kristin Boye for her help with S-XANES data analysis as well as Dr. Ann F. Marshall for help with transmission electron microscopy.

References:

1. Cornell, R. M., Schwertmann, U. (2003) *The Iron Oxides – Structure, Properties, Reactions, Occurrences and Uses*, 2nd Ed., Wiley-VCH GmbH & Co., KGaA, Weinheim, Germany, 664 p.
2. Ona-Nguema, G., Morin, G., Wang, Y., Foster, A., Juillot, F., Calas, G., Brown Jr., G. E. (2010) XANES evidence for rapid arsenic(III) oxidation at magnetite and ferrihydrite surfaces by dissolved O_2, via Fe^{2+}-mediated reactions. *Environ. Sci. Technol.* **44** (14), 5416–5422.
3. Charlet, L., Morin, G., Rose, J., Wang, Y. H., Auffan, M., Burnol, A., Fernandez-Martinez, A. (2011) Reactivity at (nano)particle-water interfaces, redox processes, and arsenic transport in the environment. *Comptes Rendus Geosci.* **343** (2-3), 123-139.
4. Brown Jr., G. E., Calas, G. (2012) Mineral-aqueous solution interfaces and their impact on the environment. *Geochem. Perspect.* **1**, 483-742.
5. Dublet, G., Juillot, F., Morin, G., Fritsch, E., Fandeur, D., Brown Jr., G. E. (2015) Goethite aging explains Ni depletion in upper units of ultramafic lateritic ores from New Caledonia. *Geochim. Cosmochim. Acta* **160**, 1-15.

6. Raiswell, R., Canfield, D. E. (2011) The iron biogeochemical cycle past and present. *Geochem. Perspect.* **1**, 1-220.

7. Nielsen, T., Andersen, F. O. (2003) Phosphorus dynamics during decomposition of mangrove (Rhizophora apiculata) leaves in sediments. *J. Exp. Marine Biol. Ecol.* **293**, 73 - 88.

8. Canfield, D. E., Kristensen, E., Thamdrup, B. (2005) *Aquatic Geomicrobiology*. Elsevier, Amsterdam, 640p.

9. Rickard, D. T. (1974) Kinetics and mechanism of the sulfidation of goethite. *Am. J. Sci.* **274**, 941-952.

10. Pyzik, A. J., Sommer, S. E. (1981) Sedimentary iron monosulfides: Kinetics and mechanism of formation. *Geochim. Cosmochim. Acta* **45**, 687-698.

11. Wei, D., Osseo-Asare, K. (1997) Aqueous synthesis of finely divided pyrite particles. *Coll. Surf.* **121**, 27-36.

12. Druhan J. L., Steefel, C I., Molins D., Williams, K. H., Conrad M. E., DePaolo, D. J. (2012) Timing the onset of sulfate reduction over multiple subsurface acetate amendments by measurement and modeling of sulfur isotope fractionation. *Environ Sci. Technol.* **46**, 8895-8902.

13. Parkman R. H., Charnock J. M., Bryan N. D., Livens F. R., Vaughan D. J. (1999) Reactions of copper and cadmium ions in aqueous solutions with goethite, lepidocrocite, mackinawite, and pyrite. *Am. Mineral*. **84**, 407–419.

14. Burton E. D., Bush R. T., Sullivan L. A. (2006) Fractionation and extractability of sulfur, iron and trace elements in sulfidic sediments. *Chemosphere* **64**, 1421–1428.

15. Marchand C., Fernandez J., Moreton B., Landi L., Lallier-Verges E., Baltzer F. (2012) The partitioning of transitional metals (Fe, Mn, Ni, Cr) in mangrove sediments downstream of a ferralitized ultramafic watershed (New Caledonia). *Chem. Geol*. **300–301**, 70–80.

16. Noël, V., Morin, G., Juillot, F., Marchand, C., Brest, J., Bargar, J. R., Muñoz, M., Marakovic, G., Ardo, S., Brown Jr., G. E. (2015) Ni cycling in mangrove sediments from New Caledonia. *Geochim. Cosmochim. Acta* **169**, 82-98.

17. Kumar, N., Chaurand, P., Rose, J., Diels, L., Bastiaens, L. (2015) Synergistic effects of sulfate reducing bacteria and zero valent iron on zinc removal and stability in aquifer sediment. *Chem. Eng. J.* **260**, 83-89.

18. Burton E. D., Bush R. T., Sullivan L. A., Johnston S. G., Hocking R. K. (2008) Mobility of arsenic and selected metals during re-flooding of iron- and organic-rich acid-sulfate soil. *Chem. Geol*. **253**, 64–73.

19. Johnston S. G., Burton, E.D., Bush, R.T., Keene, A., Sullivan, L.A., Smith, D., McElnea, A.E., Ahern, C.R., Powell, B. (2010) Abundance and fractionation of Al, Fe and trace metals following tidal inundation of a tropical acid sulfate soil. *Appl. Geochem*. **25**, 323-335.

20. Burton E. D., Bush R. T., Johnston S. G., Sullivan, L. A., Keene A. F. (2011) Sulfur biogeochemical cycling and novel Fe-S mineralization pathways in a tidally re-flooded wetland. *Geochim. Cosmochim. Acta* **75**, 3434-3451.

21. Kumar, N., Couture, R-M., Millot, R., Battaglia-Brunet, F., Rose, J. (2016) Microbial sulfate reduction enhances Arsenic mobility downstream of zero valent iron based permeable reactive barrier. *Environ. Sci. Technol.* **50**, 7610-7617.

22. Jeon, B.-H., Dempsey, B. A., Burgos, W. D., Barnett, M. O., Roden, E. E. (2005) Chemical reduction of U(VI) by Fe(II) at the solid-water interface using natural and synthetic Fe(III) oxides. *Environ. Sci. Technol.* **39**, 5642–5649.

23. Boland, D. D., Collins, R. N., Payne, T. E., Waite, T. D. (2011) Effect of amorphous Fe(III) oxide transformation on the Fe(II)-mediated reduction of U(VI). *Environ. Sci. Technol.* **45**, 1327– 1333.
24. Maher, K., Bargar, J. R., Brown Jr., G. E. (2013) Environmental speciation of actinides. *Inorg. Chem*. **52** (7), 3510-3532.
25. Rickard, D. T., Luther III, G. W. (2007) Chemistry of iron sulfides. *Chem. Rev.* **107** (2), 514−562.
26. Berner, R. A. (1984) Sedimentary pyrite formation: An update. *Geochim. Cosmochim. Acta* **48**, 605-615.
27. Rickard, D. (1995) Kinetics of FeS precipitation: Part 1. Competing reaction mechanisms. *Geochim. Cosmochim. Acta* **59**, 4367-4379.
28. Poulton, S. W. (2003) Sulfide oxidation and iron dissolution kinetics during the reaction of dissolved sulfide and ferrihydrite. *Chem. Geol.* **202**, 79-94.
29. Schoonen, M. A. A., Barnes, H. L. (1991) Reactions forming pyrite and marcasite from solution. 1. Nucleation of FeS_2 below 100-degrees-C. *Geochim. Cosmochim. Acta* **55** (6), 1495-1504.
30. Wilkin, R. T., Barnes, H. L. (1996) Pyrite formation by reactions of iron monosulfides with dissolved inorganic and organic sulfur species. *Geochim. Cosmochim. Acta* **60**, 4167–4179.
31. Rickard, D. T., Luther III, G. W. (1997) Kinetics of pyrite formation by the H_2S oxidation of iron(II) monosulfide in aqueous solution between 25 and 125°C: the mechanism. *Geochim. Cosmochim. Acta* **61**, 135–147.
32. Poulton, S. W., Krom, D. M., Raiswell, R. (2004) A revised scheme for the reactivity of iron(oxyhydr)oxide minerals towards dissolved sulfide. *Geochim. Cosmochim. Acta* **68**, 3703-3715.
33. Kumar, N., Millot, R., Battaglia-Brunet, F., Negrel, P., Diels, L., Rose, J., Bastiaens, L. (2013) Sulfur and oxygen isotope tracing in zero valent iron based in situ remediation system for metal contaminants. *Chemosphere* **90**, 1366-1371.
34. Morse J. W., Luther III, G. W. (1999) Chemical influences on trace metal-sulfide interactions in anoxic sediments. *Geochim. Cosmochim. Acta* **63**, 3373–3378.
35. Wallace, G.C., Sander, M., Chin, Y-P., Arnold, W.A. (2017) Quantifying the electron donating capacities of sulfide and dissolved organic matter in sediment pore waters of wetlands. *Environ. Sci. Process. Impact* **19**, 758-767.
36. Noël V., Marchand C., Juillot F., Ona-Nguema G., Viollier E., Marakovic G., Olivi L., Delbes L., Gelebart F., Morin G. (2014) EXAFS analysis of iron cycling in mangrove sediments downstream a lateritized ultramafic watershed (Vavouto Bay, New Caledonia). *Geochim. Cosmochim. Acta* **136**, 211–228.
37. Burton, E.D., Bush, R.T., Sullivan, L.A. (2006) Reduced inorganic sulfur speciation in drain sediments from acid sulfate soil landscape. *Environ. Sci. Technol.* **40**, 888-893.
38. Luther III, G. W. (1991) Pyrite synthesis via polysulfide compounds. *Geochim. Cosmochim. Acta* **55**, 2839-2849.
39. Wang, F. Morse, J. W. (1995) Pyrite formation under conditions approximating those in anoxic sediments: I. Pathways and morphology. *Marine Chem.* **52**, 99-121.
40. Schwertmann, U., Cornell, R. M. (2003) *Iron Oxides in the Laboratory: Preparation and Characterization.* 2nd Edition. Wiley-VCH, Weinheim, Germany, 188 p.

41. Viollier, E., Inglett, P. W., Hunter, K., Roychoudhury, A. N., Van Cappellen, P. (2000) The ferrozine method revisited: Fe(II)/Fe(III) determination in natural waters. *Appl. Geochem.* **15**, 785-790.
42. Prietzel, J., Botzaki, A., Tyufekchieva, N., Brettholle, M., Thieme, J., Klysubun, W. (2011) Sulfur speciation in soil by S K-Edge XANES spectroscopy: comparison of spectral deconvolution and linear combination fitting. *Environ. Sci. Technol*. **45** (7), 2878–2886
43. Ravel, B., Newville, M. (2005) Athena, Artemis, Hephaestus: Data analysis for X-ray absorption spectroscopy using IFEFFIT. *J. Synchrotron Rad.* **12**, 537-541.
44. Fleet M. E. (2005) XANES spectroscopy of sulfur in earth materials. *Can. Mineral.* **43**, 1811-1838.
45. Noël, V., Boye, K., Kukkadapu, R. K., Bone S., Lezama-Pacheco, J. S., Cardarelli, E., Janot, N., Fendorf, S., Williams, K. H., Bargar J. R. (2017) Understanding controls on redox processes in floodplain sediments of the Upper Colorado River Basin. *Sci. Total Environ.* **603-604**, 663-675.
46. Wasserman, S. R., Allen, P. G., Shuh, D. K., Bucher, J. J., Edelstein, N. M. (1999) EXAFS and principal component analysis: a new shell game. *J. Synchrotron Rad*. **6** (3), 284-286.
47. Webb, S. M. (2005) SIXPack: A graphical user interface for XAS analysis using IFEFFIT. *Physica Scripta* **T115**, 1011-1014.
48. Malinowski, E. R. (1977) Determination of the number of factors and the experimental error in a data matrix. *Anal. Chem*. **49** (4), 612-617.
49. Prietzel, J., Thieme, J., Tyufekchieva, N., Paterson, D., McNulty, I., Kögel-Knabner, I. (2009) Sulfur speciation in well-aerated and wetland soils in a forested catchment assessed by sulfur K-edge X-ray absorption near-edge spectroscopy (XANES). *J. Plant Nutr. Soil Sci.* **172** (3), 393–403.
50. Ankudinov, A. L., Ravel, B., Rehr, J. J., Conradson, S. D. (1998) Real-space multiple-scattering calculation and interpretation of x-ray-absorption near-edge structure. *Phys. Rev. B* **58**, 7565.
51. Michel, F. M., Ehm. L., Antao, S. M., Lee, P. L., Chupas, P. J., Liu, G., Strongin, D. R., Schoonen, M. A., Phillips, B. L., Parise, J. B. (2007) The structure of ferrihydrite, a nanocrystalline material. *Science* **316**, 1726-1729.
52. Maillot F., Morin G., Wang Y., Bonnin D., Ildefonse P., Chaneac C., Calas G. (2011) New insight into the structure of nanocrystalline ferrihydrite: EXAFS evidence for tetrahedrally coordinated iron (III). *Geochim. Cosmochim. Acta* **75** (10), 2708– 2720.
53. Wilke, M., Farges, F., Petit, P-E., Brown Jr., G. E., Martin, F. (2001) Oxidation state and coordination of Fe in minerals: An Fe *K*-XANES spectroscopic study. *Am. Mineral.* **86**, 714-730.
54. Farges, F., Lefrere, Y., Rossano, S., Berthereau, A., Calas, G., Brown Jr., G. E. (2004) The effect of redox state on the local structural environment of iron in silicate glasses: a combined XAFS spectroscopy, molecular dynamics, and bond valence study. *J. Non-Crystal. Solids* **344**, 176–188.
55. Ikogou, M., Ona-Nguema, G., Juillot, F., Le Pape, P., Menguy, N., Richeux, N., Guigner, J-M., Noël, V., Brest, J., Baptiste, B., Morin, G. (2017) Long-term sequestration of nickel in mackinawite formed by *Desulfovibrio capillatus* upon Fe(III)-citrate reduction in the presence of thiosulfate. *Appl. Geochem.* **80**, 143-154.

56. Lennie, A., Redfern, S., Schofield, P., and Vaughan, D. J. (1995) Synthesis and Rietveld crystal structure refinement of mackinawite, tetragonal FeS. *Mineral. Mag*. **59**, 677–683.
57. Davison, W., Phillips, N., Tabner, B.J. (1999) Soluble iron sulfide species in natural waters: reappraisal of their stoichiometry and stability constants. *Aquatic Sci.* **61**, 23-43.
58. Wilkin, R.T., Beak, D.G. (2017) Uptake of nickel by synthetic mackinawite. *Chem. Geol.* **462,** 15-29.
59. Torrent, J., Schwertmann, U., Barron, V. (1987) The reductive dissolution of synthetic goethite and hematite in dithionite. *Clay Mineral*. **22**, 329-337.
60. Larsen, O., Postma, D. (2001) Kinetics of reductive bulk dissolution of lepidocrocite, ferrihydrite, and goethite. *Geochim. Cosmochim. Acta* **65** (9), 1367-1379.
61. Trainor, T. P., Chaka, A. M., Eng, P. J., Newville, M., Waychunas, G. A., Catalano, J. G., Brown Jr., G. E. (2004) Structure and reactivity of the hydrated hematite (0001) surface. *Surf. Sci.* **573**, 204-224.
62. Ghose, S. K., Waychunas,G. A., Trainor, T. P., Eng, P. J. (2010) Hydrated goethite (α–FeOOH) (001) interface structure: Ordered water and surface functional groups. *Geochim. Cosmochim. Acta* **74**, 1943-1953.
63. Canfield D. E., Raiswell R., Bottrell S. (1992) The reactivity of sedimentary iron minerals toward sulfide. *Am. J. Sci*. **292**, 659-683.
64. Levard, C. M., Hotze, M., Lowry, G.V., Brown Jr., G. E. (2012) Environmental transformations of silver nanoparticles: Impact on stability and toxicity. *Environ. Sci. Technol.* **46**, 6900-6914.
65. Ma, R., Levard, C., Michel, F.M. Brown Jr., G. E., Lowry, G. V. (2013) Sulfidation mechanism for zinc oxide nanoparticles and the effect of sulfidation on their solubility. *Environ. Sci. Technol.* **47** (6), 2527-2534.
66. Malinowski E. R. (1978) Theory of error for target factor analysis with applications to mass spectrometry and nuclear magnetic resonance spectrometry. *Anal. Chim. Acta* **103**, 339-354.
67. Ndiba, P., Axe, L., Boonfueng, T. (2008) Heavy metal immobilization through phosphate and thermal treatment of dredged sediments. *Environ. Sci. Technol*. **42**, 920-926.
68. Janot, N., Lezama-Pacheco, J. S., Pham, D. Q., O'Brien, T. M., Hausladen, D., Noël, V., Lallier, F., Maher, K., Fendorf, S., Williams, K. H., Long, P. E., Bargar, J. R. (2015) Physico-chemical heterogeneity of organic-rich sediments in the Rifle aquifer, CO: Impact on uranium biogeochemistry. *Environ. Sci. Technol.* **50** (1), 46-53.
69. Paquette, K. E., Helz, G. R. (1997) Inorganic speciation of mercury in sulfidic waters: The importance of zero-valent sulfur. *Environ. Sci. Technol*. **31**, 2148-2153.
70. Schoonen, M. A. A. (2004) Mechanisms of sedimentary pyrite formation. *GSA Special Paper* **379**, 117-134.
71. Luther III, G. W. (1990) The frontier-molecular orbital theory approach in geochemical processes. In *Aquatic Chemical Kinetics* (ed. W. Stumn), Wiley, NY, pp. 173-198.
72. Dos Santos Alfonso, M., Stumm, W. (1992) Reductive dissolution of iron(III) (hydr)oxides by hydrogen sulfide. *Langmuir* **8**, 1671-1675.
73. Jeon, B. H., Dempsey, B. A., Burgos, W. D. (2003) Kinetics and mechanisms for reactions of Fe(II) with iron (III) oxides. *Environ. Sci. Technol.* **37**, 3309-3315.

74. Handler, R. M., Beard, B. L., Johnson, C. M., Scherer, M. M. (2009) Atom exchange between aqueous Fe(II) and goethite: An Fe isotope tracer study. *Environ. Sci. Technol.* **43** (4), 1102-1107.

75. Peiffer, S., Gade, W. (2007) Reactivity of ferric oxides toward H_2S at low pH. *Environ. Sci. Technol.* **41**, 3159-3164.

76. Kornicker, W. A., Morse, J. W. (1991) The interactions of divalent cations with the surface of pyrite. *Geochim. Cosmochim. Acta* **55**, 2159-2172.

77. Johnston, S. G., Slavich, P. G., Hirst, P. (2004) The acid flux dynamics of two artificial drains in acid sulfate soil backswamps on the Clarence River floodplain, Australia. *Aust. J. Soil Res.* **42**, 623–637.

78. Claff, S. R., Burton, E. D., Sullivan, L. A., Bush, R. T. (2011) Metal partitioning dynamics during the oxidation and acidification of sulfidic soil. *Chem. Geol.* **286**, 146-157.

79. Nath, B., Birch, G., Chaudhuri, P. (2013) Trace metal biogeochemistry in mangrove ecosystems: A comparative assessment of acidified (by acid sulfate soils) and non-acidified sites. *Sci. Total Environ*. **463–464**, 667–674.

80. Machado, W., Borrelli, N. L., Ferreira, T. O., Marques, A. G. B., Osterrieth, M., Guizan, C. (2014) Trace metal pyritization variability in response to mangrove soil aerobic and anaerobic oxidation processes. *Mar. Pollut. Bull.* **79** (1-2), 365-70.

81. Widler, A.M., Seward, T.M. (2002) The adsorption of gold(I) hydrosulphide complexes by iron sulphide surfaces. *Geochim. Cosmochim. Acta* **66**, 383-402.

82. Dublet, G., Pacheco, J.L., Bargar, J.R., Fendorf, S., Kumar, N., Lowry, G.V., Brown Jr., G.E. (2017) Partitioning of uranyl between ferrihydrite and humic substances at acidic and circum-neutral pH. *Geochim. Cosmochim. Acta* **215**, 122-140.

83.Kosmulski, M., Maczka, E., Jartych, E., Rosenholm, J.B. (2003) Synthesis and characterization of goethite and goethite-hematite composite: experimental study and literature survey. *Adv. Colloid Interface Sci.* **103**, 57-76.